Eleventh International Conference on Computational Fluid Dynamics (ICCFD11), Lahaina, USA, July 11-15, 2022

ICCFD11-2022-2004

Numerical Investigation of a Bio-Inspired Airfoil with Air-Permeable Holes

E. Tangermann*, G. Ercolani* and M. Klein*
Corresponding author: eike.tangermann@unibw.de

* University of the Bundeswehr Munich, Germany

Abstract: An airfoil derived from a bird's primary feather has been investigated numerically at low Reynolds number conditions ($Re = 30000$). It features two rows of holes along its shaft, through which air is passing driven by the pressure difference between the lower and the upper side. This air flow interacts with the separated shear layer on the upper side and affects the transition process within the shear layer. By means of DNS, this process has been assessed for different angles of attack which provide different flow conditions around the feather in terms of separated and attached flow regions. At higher angles of attack, the shear layer is affected in a way that it bends towards the surface allowing a higher level of suction and consequently an increase of lift. The flow rate through the hole rows is compared to findings from literature to allow a qualitative validation of the simulation setup.
Keywords: Computational Fluid Dynamics, Aerodynamics, Biomimetics.

1 Introduction

The flow around bird's feathers features a variety of complex phenomena arising from the geometrical structure of the feather evolved from the evolutionary process which are exposed to low Reynolds numbers. The surface of a feather can be considered rough to a certain extent. It is, however, not a homogeneous and isotropic roughness of sand type but dominated by distinct structures. Further, the feathers are permeable and do not form a closed surface. This becomes relevant in particular for the primary feathers at the wing tip, which experience flow on both sides as they are not covered by other parts.

Many bird species feature a cascade of primary feathers designed to gain lift by splitting the tip vortex into smaller vortices and thereby reduce the induced drag. The mechanism has been described from experimental as well as numerical investigations [1, 2, 3, 4, 5]. In the wind tunnel experiments, actual birds have been employed, whereas the numerical analysis has been built upon simplified models, neglecting roughness and permeability of the feathers and concentrating on the flow features at larger scales. As the flow Reynolds number on a primary feather typically is between 10000 and 40000, the numerical study with smooth and solid feathers has shown significant regions of flow separation, where the laminar flow is not able to follow the curvature of the feather. It has been concluded, that both roughness and permeability will have a significant effect on the separation behavior and therefore should be accounted for in further work.

The effect of permeability on a primary feather has been described by Eder et al. [6], who have performed measurements of the flow rate passing through a feather. According to its structure, the feather permeability can be classified in two different ranges. Along the shaft (rachis) between the roots of the barbs (rami), holes remain open as will be discussed below in the geometry description. Here the flow can pass at a higher flow rate. Within the vanes, the barbs are connected by the barbules forming a more closed surface, which still is permeable but to a lower extent. The area specific flow rate through the holes is significantly higher than the one through the vanes. However, it needs to be kept in mind, that the vanes feature a far higher surface area and thereby also have a significant amount of flow passing. Nonetheless, the momentum through the holes is expected to be higher and thus the effect by these micro-jets is different from the diffusion-like flow through the barbs.

Figure 1: Feather airfoil designed from tomographic material by Eder et al.[6].

Figure 2: View to the entire feather from the lower side.

In the numerical simulation of an entire feather or even a wing, none of these effects can be fully resolved due to the enormous required computational effort. In order to develop suitable models for large-scale applications, the effects need to be separated and studied individually. Within the present study, only the permeability of the hole rows is investigated in an isolated way. Fully resolving simulation results from a planar configuration are presented. Both the flow through the holes as well as its effect on the surrounding flow field and the aerodynamic properties are discussed.

2 Geometrical Model

Within their work [6], Eder et al. have presented airfoil sections of a white stork's primary feather which have been obtained from tomographic images of a feather exposed to variable load states. Based on this data, the solid feather geometry for the present study has been designed. Figure 1 shows the base airfoil. It features a maximum camber of 10.2% at a depth of 32.9%, which according to Eder et al. is associated with operation under high load rather than efficient gliding. In the present study, the focus is set to operation at high lift as here the flow through the holes, flow separation and their interacting effects are expected to be stronger. The maximum thickness of the airfoil is 6.2% within the shaft. In the external and internal vanes the maximum thickness is 4.8% and 3.4%, respectively. The sharp leading edge is a typical feature of airfoils operating at low Reynolds numbers.

Figure 2 shows a white stork's feather on which the small scale features of the geometrical model are based. Considering its depth of approximately $c = 45mm$ and an airspeed in soaring flight of $V = 10m/s$, the Reynolds number results in $Re = 30000$. A slice approximately corresponding to Figure 3 has been extracted as a planar configuration with periodic conditions in span-wise direction.

Figure 3 provides an impression of the hole structure formed on both sides between the barbs where they are connected to the shaft from a macroscopic perspective. In the external vane (vexillum externum), the barbs are arranged in a different way than in the internal vane (vexillum internum). In the former they are arranged less dense and bent in a more acute angle. The holes formed thereby are longer than those on the internal vane but also thinner and result in a very similar cross-sectional area but a different shape. On the upper side the barbs become thicker and hence the holes become narrower. Besides the hole regions the barbs are closer together but still leave thin open slots, through which air can pass, which is not considered in the present study in order to isolate the effect. The barbs are connected by barbules. They might have a slight damping effect which, however, has been neglected in the present study.

The shape of the holes extracted from microscopic images has been projected onto the upper and lower sides of the planar wing model. A slight modification has been applied to achieve the desired periodicity of the hole patterns on both sides of the shaft. The resulting geometrical model is shown in Figure 4 from different

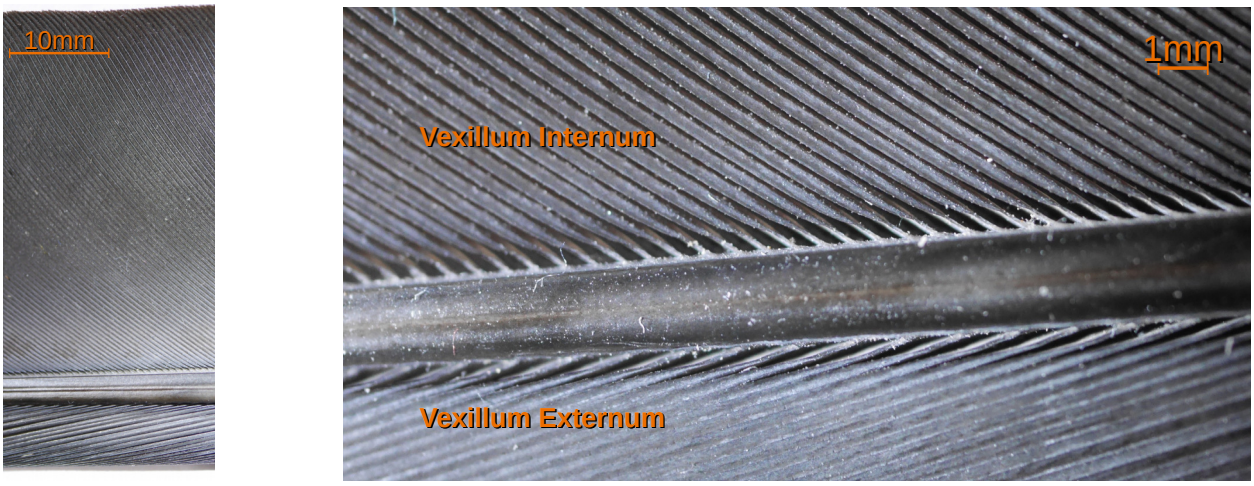

Figure 3: Enlarged view to a strip of the feather approximately corresponding to the simulated domain (left). Macroscopic view to the holes on both sides of the shaft from the lower side (right).

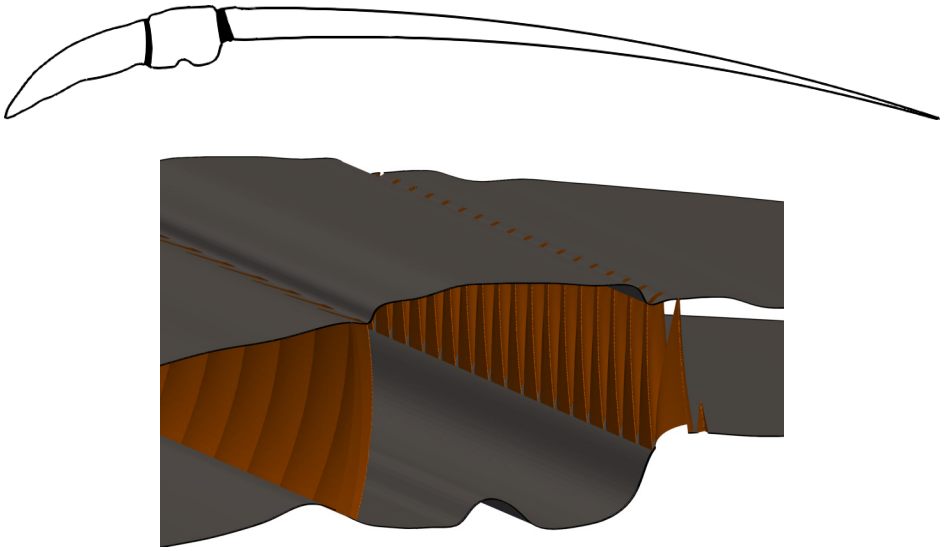

Figure 4: Geometry of the planar wing with holes. 2D section (top) and close-up of the hole structure in 3D (bottom).

perspectives. In dimensionless values, the front row holes feature a sectional area of $A/c^2 = 13.5 \cdot 10^{-5}$ on the lower side which decreases to a value of $5.2 \cdot 10^{-5}$ on the upper side. The aft row holes range from $A/c^2 = 15.4 \cdot 10^{-5}$ on the lower side to $4.2 \cdot 10^{-5}$ on the upper side. Since the aft row features twice as many holes per span as the front row, the resulting flow rate also is higher as will be shown below.

3 Numerical Method

All simulations have been performed using the OpenFOAM flow solver toolbox. For a preliminary study, first two-dimensional RANS simulations with the solid model have been performed to identify the operational range of interest. Based on these results, four angles of attack have been selected to perform DNS computations. An incompressible formulation of the Navier-Stokes equations has been employed. Pressure

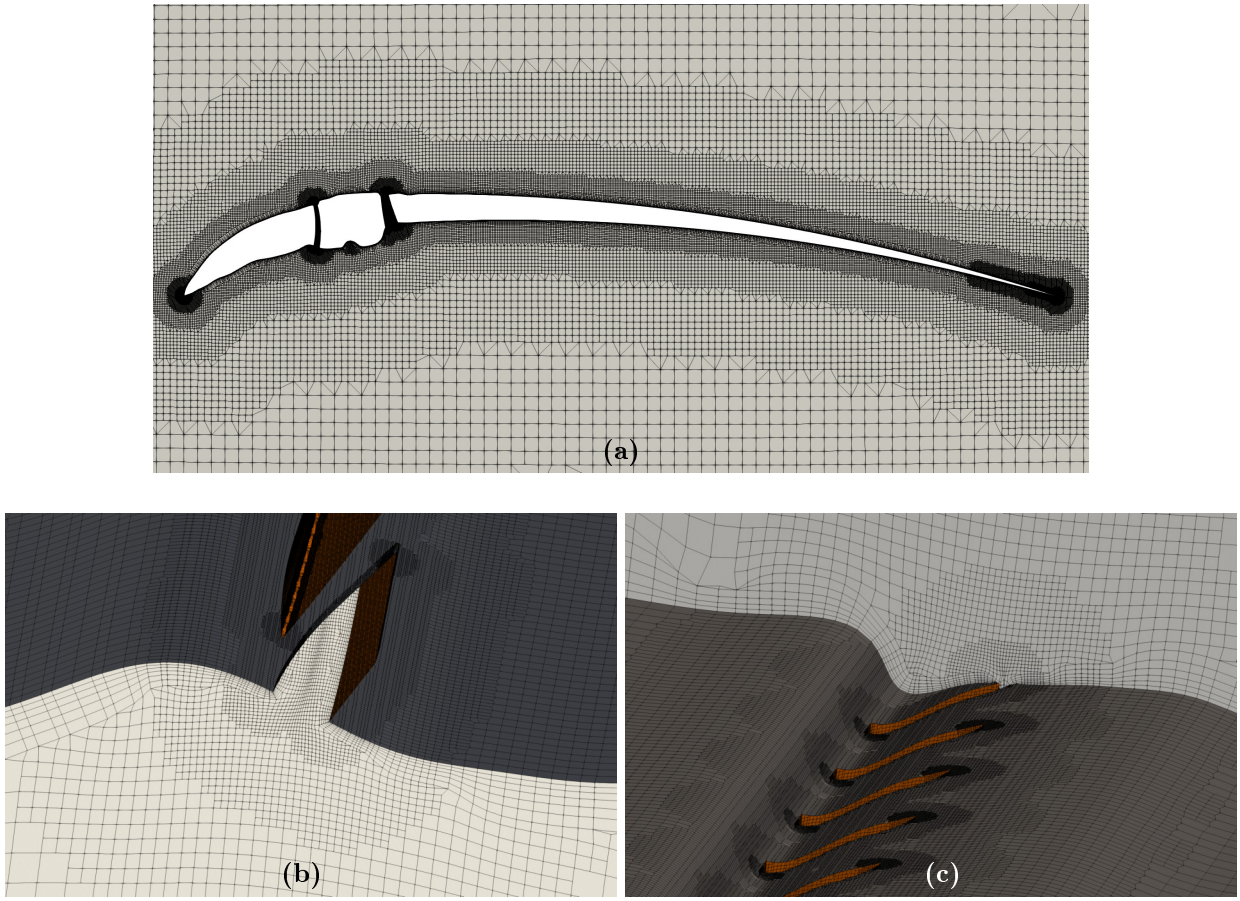

Figure 5: Computational mesh of the wing with holes. (a) xz-plane from periodic boundary, (b) hole inlet on lower side, (c) hole outlet on upper side.

and velocity coupling has been achieved by PISO time stepping with inner iterations of SIMPLE type. For temporal discretization a second order accurate backward scheme has been used. In the case of DNS, the spatial discretization is of second order central type blended with a minimal amount of second order upwind to ensure stability with the complex mesh structure.

For the RANS computations, the SST turbulence model [7] supplemented with the γ-Re_θ transition model [8] has been selected. Due to the low Reynolds number, significant parts of the flow are laminar which must be considered by the turbulence model. However, the behavior of the separated and turbulent shear layer above the internal vane dominates the aerodynamic properties and this part of the flow cannot be predicted sufficiently accurate by RANS. Therefore, the RANS results are only applicable in the assessment of incoming flow to the leading edge and for identifying the location of flow separation.

The computational mesh is based on hierarchically refined hexahedra. To avoid hanging nodes, interface layers formed of polyhedra are situated between the refinement levels. The outer boundary of the computational domain is of farfield type and located 50 times the chord length c from the wing. In span-wise direction the solid geometry extends 0.25 times the chord length with periodic coupling, which has been found sufficient in simulations of comparable wings [9]. The wing with holes is slightly wider with a span of $0.261c$ in order to fit the periodicity of the of the hole patterns.

Towards the wing, cell layers are introduced for an appropriate resolution of the boundary layer. The spacing of the first cell is well below $y^+ < 1$ to capture the wall normal gradients. Along the wall the spacing of x^+ and z^+ reaches a maximal value of 8 in the front part but remains below 5 in the turbulent parts of the boundary layers, which is sufficient to resolve all turbulent structures. The processes of flow separation

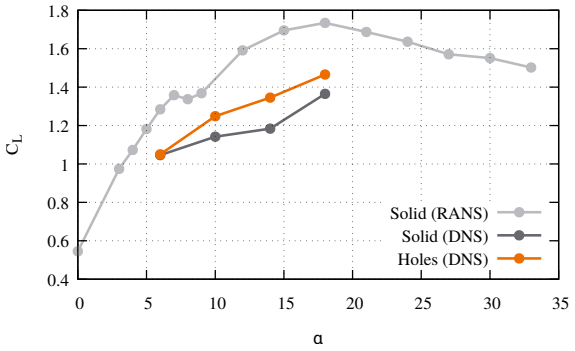

Figure 6: Lift produced by the airfoil with and without holes over angle of attack.

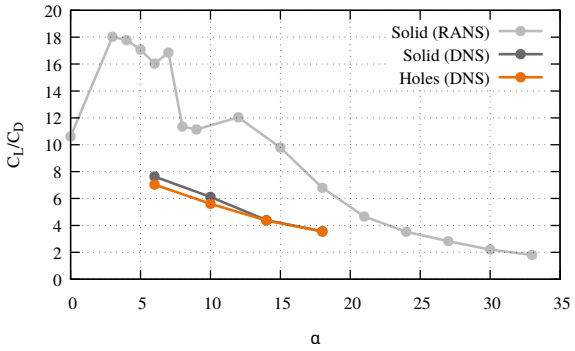

Figure 7: Glide efficiency C_L/C_D of the planar airfoil over angle of attack.

and the consequent breakup of the separated shear layer also take place in cells fine enough to adequately resolve them.

A further refinement is required to resolve the flow through the holes. An impression is given from the plots in Figure 5 showing the inlet and outlet regions of the aft row of holes. Besides the fine cells, wall layers also are applied inside the holes to resolve the boundary layers. With fully resolved holes, the mesh consists of a total of $39.7 \cdot 10^6$ cells, whereas the solid wing only requires $28.6 \cdot 10^6$ cells.

4 Results and Discussion

A series of 2D RANS computations has been performed in a preliminary step as mentioned above in order to identify relevant ranges for the angle of attack. The sharp leading edge has an optimal angle for the approaching flow, where the stagnation point is situated on the leading edge. A deviation from this condition leads to a flow separation on the upper or lower side. For the present airfoil, this condition is achieved for an angle of attack of $\alpha = 7°$. At smaller values the flow separates on the lower side immediately at the leading edge and re-attaches downstream of the shaft. On the upper side it initially remains attached but then separates after passing the shaft even at these low angles of attack.

Figures 6 and 7 show the development of lift and of glide efficiency, respectively. As mentioned above, the results from RANS are to be considered qualitatively only in this context, as the method is barely capable of predicting this type of flow sufficiently accurate. Best glide efficiency is achieved around $\alpha = 3°$. However, the airfoil rather is designed for high lift than for high efficiency following the observations by Eder et al. [6]. A local maximum of lift is achieved for $\alpha = 7°$ when the leading edge is approached ideally and the flow attaches on the lower side. When increasing α, the separation on the upper side starts moving further upstream and both lift and efficiency decrease. With further increasing α, lift also increases at reduced efficiency until maximal lift is achieved for $\alpha = 18°$. Within this range, four different angles of attack have been selected with different states of the flow. Starting from $\alpha = 6°$, at reasonably good glide efficiency and separated flow on the lower side, the angle of attack is increased in steps of 4° to $\alpha = 10°$, $\alpha = 14°$ and finally to maximum lift at $\alpha = 18°$.

For each of the cases DNS computations with and without holes have been performed. The results for lift and efficiency are shown in Figures 6 and 7 as well. At the two lower angles of attack the glide efficiency is slightly decreased by the holes, whereas for higher α the holes seem to have no impact on the efficiency. On the other hand, the lift is affected by the flow through holes in the cases of higher α. For the first case, in which the flow separates below the leading edge, the lift is almost identical. When the stagnation point moves to the lower side and the flow is attached, the lift increases significantly.

The origin of increased lifting force can be found in the pressure distribution on the upper side of the wing. Figure 8 shows pressure and friction along the wing surface for all considered cases. On the upper side, a slightly decreased suction appears in the front part for $\alpha = 6°$. In the aft part, the pressure is almost identical. In this case, the strongest impact of the holes can be seen in the front part of the lower side, where

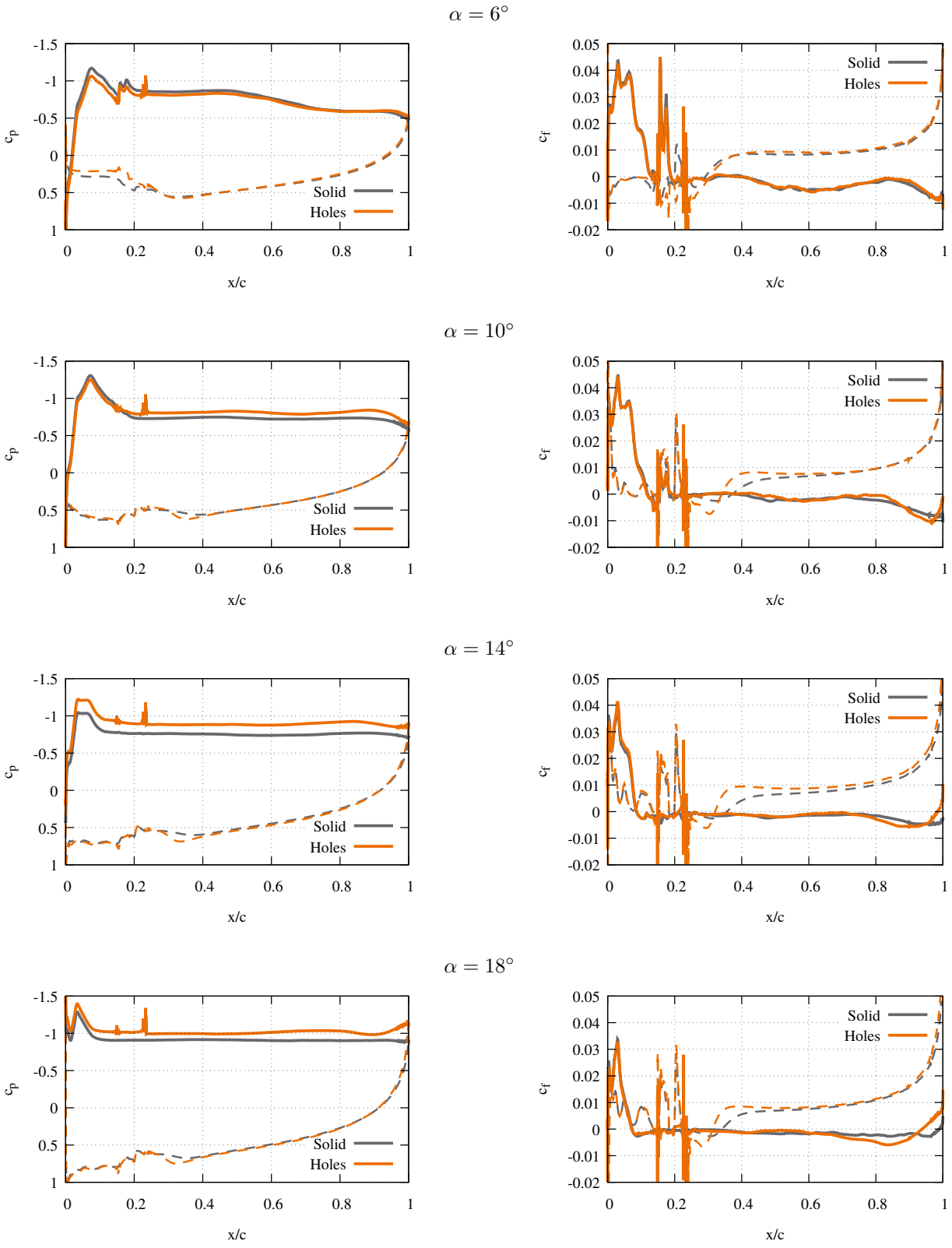

Figure 8: Pressure (left) and surface friction (right) coefficients. Solid lines indicate upper side, dashed lines lower side.

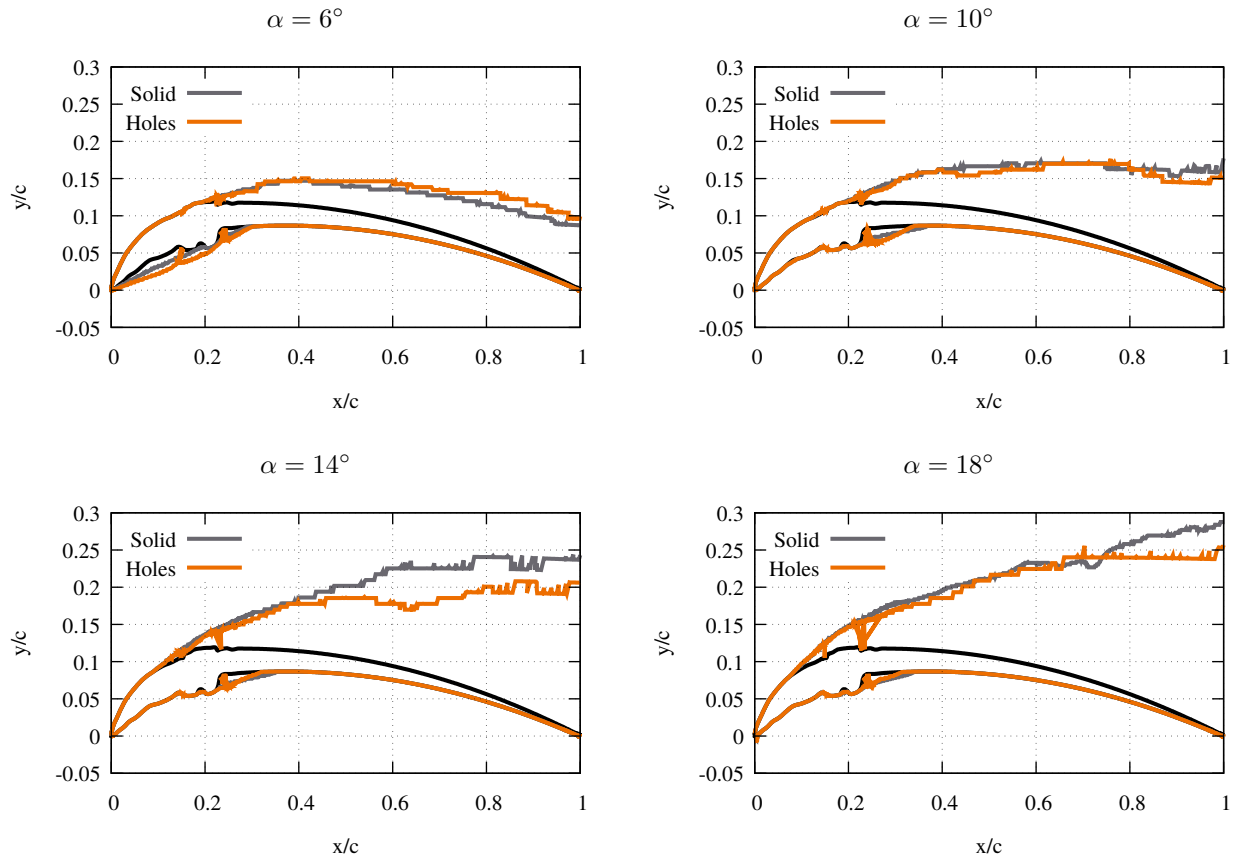

Figure 9: Regions of reversed flow around the wing to indicate flow separation marked by iso-lines of zero stream-wise mean velocity.

the pressure is reduced in the separated area. The separated regions, however, are not affected as can be seen from the friction coefficient. Only in an isolated zone around the holes on the lower side (dashed lines around $x/c = 0.2$), significant differences are visible. The friction coefficient further underlines that the flow is separated along most of the upper side. It drops to negative values at the shaft and remains negative until reaching the trailing edge. Consequently, the pressure along the upper side remains almost constant while the flow is separated.

All other angles of attack show an increased suction for the wing with holes. At $\alpha = 10°$, this effect appears only in the aft part of the wing. Its onset approximately coincides with the first flow separation very slightly upstream of the shaft. For the two higher angles of attack, the upper side suction is higher almost from the leading edge on. On the lower side, the pressure is almost identical in both configurations as soon as the leading edge separation disappears. Only a slight difference occurs between $x/c = 0.3$ and 0.4 downstream of the shaft, where the wing with holes produces a slightly higher pressure. This phenomenon is connected with differences in the flow separation around the shaft as can be seen in the plots of the friction coefficient. Up to $x/c = 0.3$ the holes cause a stronger negative friction but then the flow attaches far sooner and the friction coefficient reaches higher values than on the solid wing. As will be discussed below, the flow bleeding through the aft holes slightly changes the flow topology and allows turbulence to be generated below the external vane.

Another perspective to the flow processes around the wing is provided by the regions of reversed flow shown in Figure 9, surrounded by iso-lines of zero stream-wise mean velocity. In all cases, the first separation on the upper side occurs in the same way independently of the holes, but the following recirculation zone shows differences. At $\alpha = 6°$, the recirculation becomes marginally thinner immediately after passing the second hole row but then shows an increased thickness in the aft part of the wing. On the lower side,

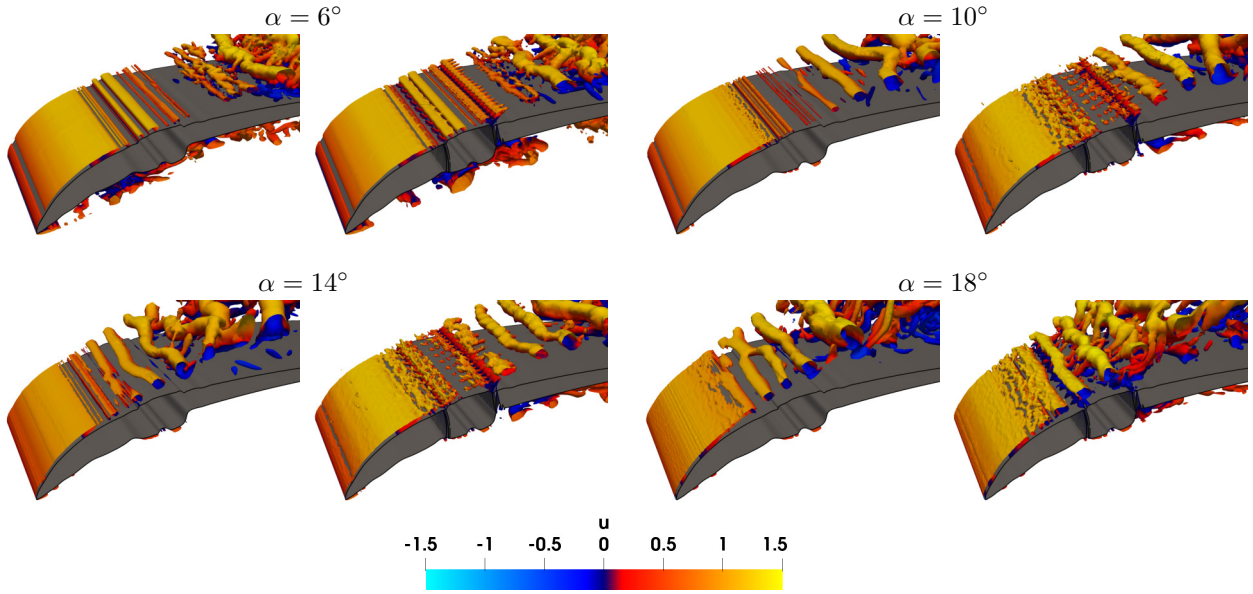

Figure 10: Onset of the shear layer separation by iso-surfaces of instantaneous Q-criterion colored by stream-wise velocity u. For each angle of attack solid wing (left) and wing with holes (right).

the wing with holes also has a thicker zone of reversed flow. For the higher angles of attack this behavior changes. On the lower side, as discussed above from the friction coefficient, the separation behind the shaft becomes slightly smaller. The main effect, however, appears on the upper side. After passing the holes, the recirculation zone becomes thinner, first only slightly but further towards the trailing edge the effect becomes stronger.

This impact on the recirculation is caused by the flow through the holes which interacts with the shear layer and affects its breakup into smaller structures. The onset of the shear layer separation above the reversed flow is shown in Figure 10. Iso-surfaces of Q-criterion are provided for the different angles of attack from both wings without and with holes. The surfaces are colored by stream-wise velocity to indicate regions of instantaneously reversed flow. It can be seen that shear layer vortices of Kelvin-Helmholtz type are formed upon the separation. On the solid wings, they begin as two-dimensional structures and slowly break up into three-dimensional turbulence. At $\alpha = 6°$ the separation only occurs after passing the shaft. When increasing the angle of attack to $\alpha = 10°$, the separation moves upstream to the front edge of the shaft, which acts as a step forcing the flow to separate. At even higher angles of attack, the flow already separates upstream of the shaft and the vortices experience breakup sooner after separation.

For all cases with holes, the disturbance of the jets coming from the holes is obvious in the Q isosurfaces. Already at $\alpha = 6°$ wrinkled structures appear when the flow passes the first hole raw. Since it is still attached, these disturbances are damped quickly by the proximity of the wall. After passing the second hole raw, the jets mix into the shear layer and introduce smaller structures, which then have an impact on the transition. At $\alpha = 10°$ the effect is stronger and already is visible slightly upstream of the first hole row. Downstream of the second row, the shear layer vortex is superimposed with small vortical structures which then tend to decay until the large vortices start to break up. This process is similar for $\alpha = 14°$. As shown above, the separation upstream of the shaft is still present in this case. It, however, is already affected by small scale structures even upstream of the holes. The recirculating regions are split by the flow from the holes, therefore the shear layer develops differently. After passing the second hole row, again small structures are visible within the now forming Kelvin-Helmholtz vortices. The small structures then even tend to decay while the shear layer vortices are growing. As the shear layer is interrupted above the holes, the actual transition into turbulence is delayed since the Kelvin-Helmholtz vortices establish further downstream and only then the transition can occur. The small structures are too weak to enhance breakup and transition. The opposite happens for $\alpha = 18°$. Here the shear layer already becomes turbulent while passing the first hole row. The Kelvin-Helmholtz vortices do not recover but already start breaking up excited by the jets.

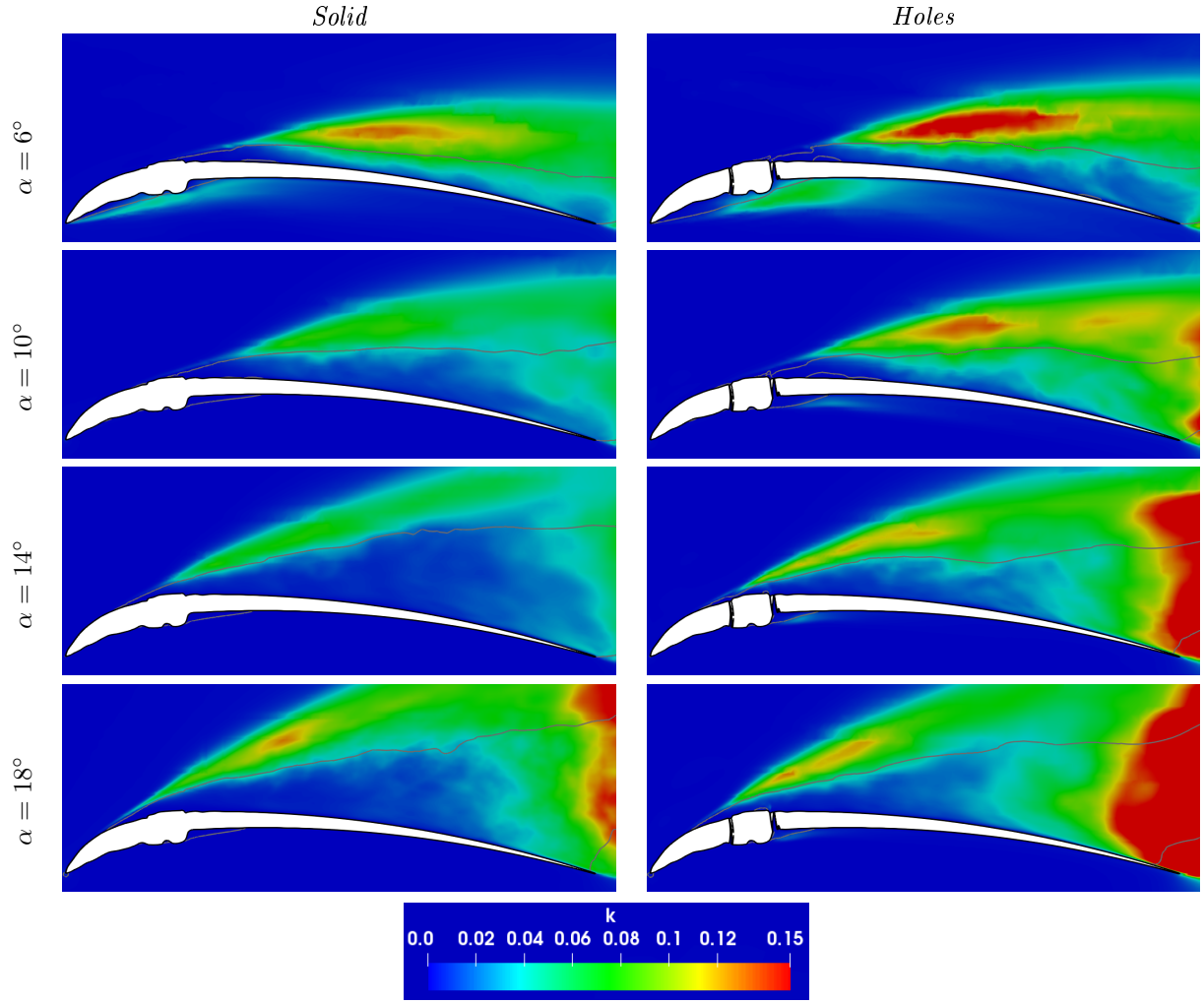

Figure 11: Mean turbulence kinetic energy k around the wing. The black line indicates the region of reversed flow.

The solid feather, whereas, shows the large vortices reaching further downstream before they break up.

Figure 10 also gives an impression of the turbulence on the lower side of the wing. For the lowest angle of attack where the flow separates below the leading edge, turbulent structures appear along the entire lower side slowly decaying towards the trailing edge. Their onset can be seen in the images. The three higher angles of attack do not lead to turbulence in the front part of the lower side. As shown above, the solid wing experiences some separation on the lower side behind the shaft. This, however, does not lead to turbulent flow but only creates a laminar recirculation whereas the configuration with holes produces significant turbulent structures in these cases. They appear downstream of the shaft. This corresponds to the different shape of the separation zone and the surface friction discussed above. The flow exiting this region through the holes is suspected to cause this behavior. It intensifies the wall-normal velocity gradients as the approaching flow needs to fill the region. Thus, transition is achieved and turbulent structures are formed. This also slightly accelerates the re-attachment of the flow.

Figure 11 gives an impression of the fluctuation intensity by contours of the averaged turbulence kinetic energy. The effect of the turbulence on the lower side can be seen for all cases as discussed for the instantaneous views. More obvious is the difference between the turbulence fields on the upper side. In all cases, the holes increase the turbulence intensity significantly. The effect appears most for the lower angles of attack. Upon breakup of the shear layer vortices, a local maximum of turbulence energy appears. The absolute maximum is reached downstream of the wing in the onset of the wake flow which, however, is of

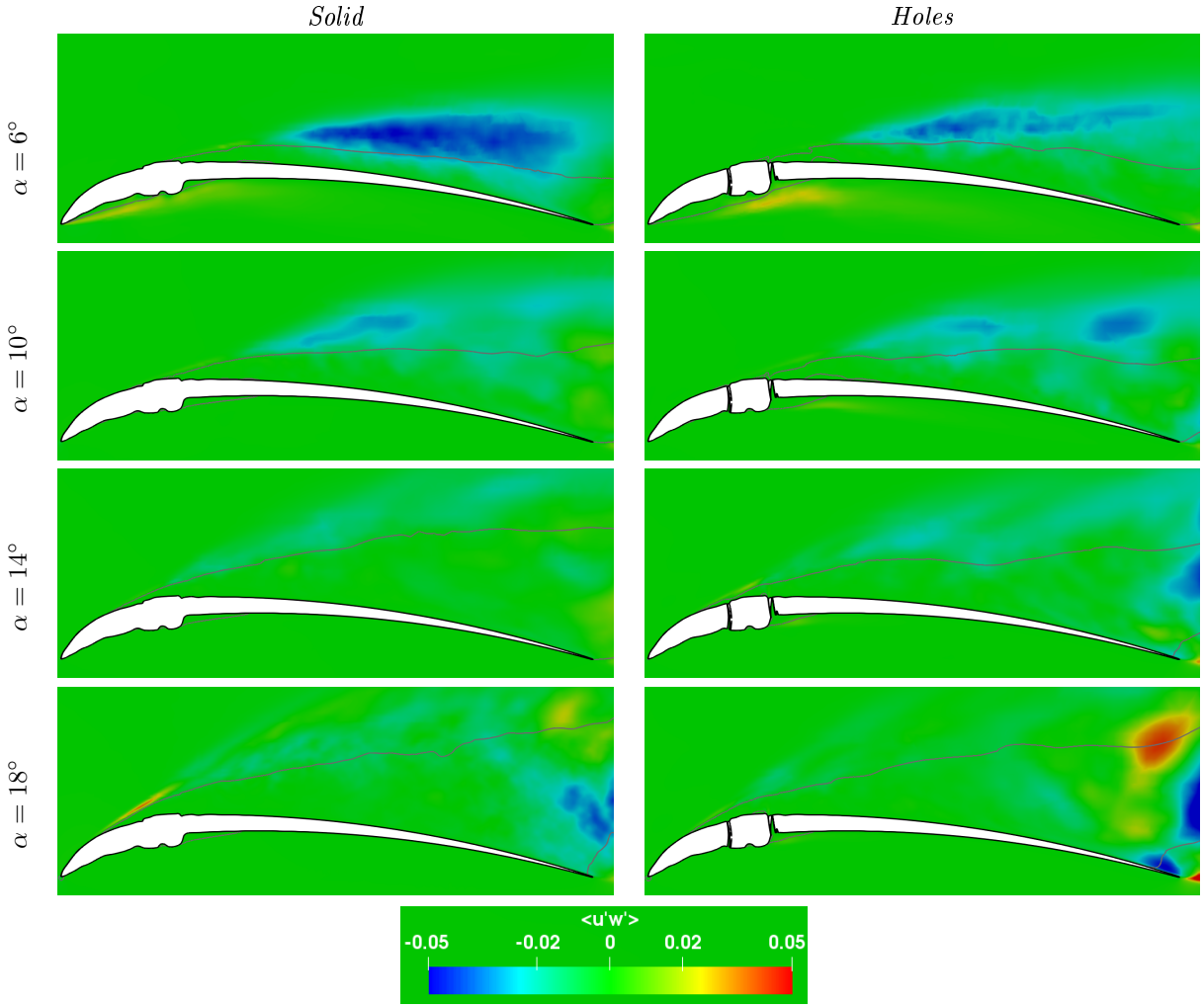

Figure 12: Mean Reynolds shear stress $u'w'$ around the wing. The black line indicates the region of reversed flow.

less importance for the present investigation.

The structures seen in the instantaneous fields exciting the shear layer above the holes do not appear in the averaged plots as they have small scales and do not carry much energy. The Kelvin-Helmholtz vortices leave noticeable footprints in terms of turbulence energy when they grow in diameter and of course when they break up into three-dimensional turbulent structures.

For another perspective to the turbulence field, contour plots of mean Reynolds shear stress $u'w'$ are provided in Figure 12, where u denotes the chord-wise and w the vertical direction. Here the solid wing shows a significantly higher level of intensity magnitude. As in this shear layer configuration high negative levels can be associated with a damping effect on the turbulence intensity, the weaker damping observed with the holes explains the increased turbulence intensity seen before. Hence, the jets from the holes, as suspected from the instantaneous plots, actually have a stabilizing effect on the shear layer vortices. The effect is strongest for the two lower angles of attack, where the flow separates behind or on the shaft.

In the two cases of higher α with separation upstream of the shaft, the magnitude of $u'w'$ generally decreases. The trend of reduced $u'w'$ by the holes remains but is hardly visible in Figure 12. Now a region of higher turbulence energy appears in the shear layer immediately after passing above the holes as clearly visible in Figure 11, which presumably is connected with excitation be the jets.

For a closer view of how the flow passes the holes, Figure 13 shows streamlines based on the averaged flow field passing around the leading edge and through the holes. In principle, the mean flow field is statistically

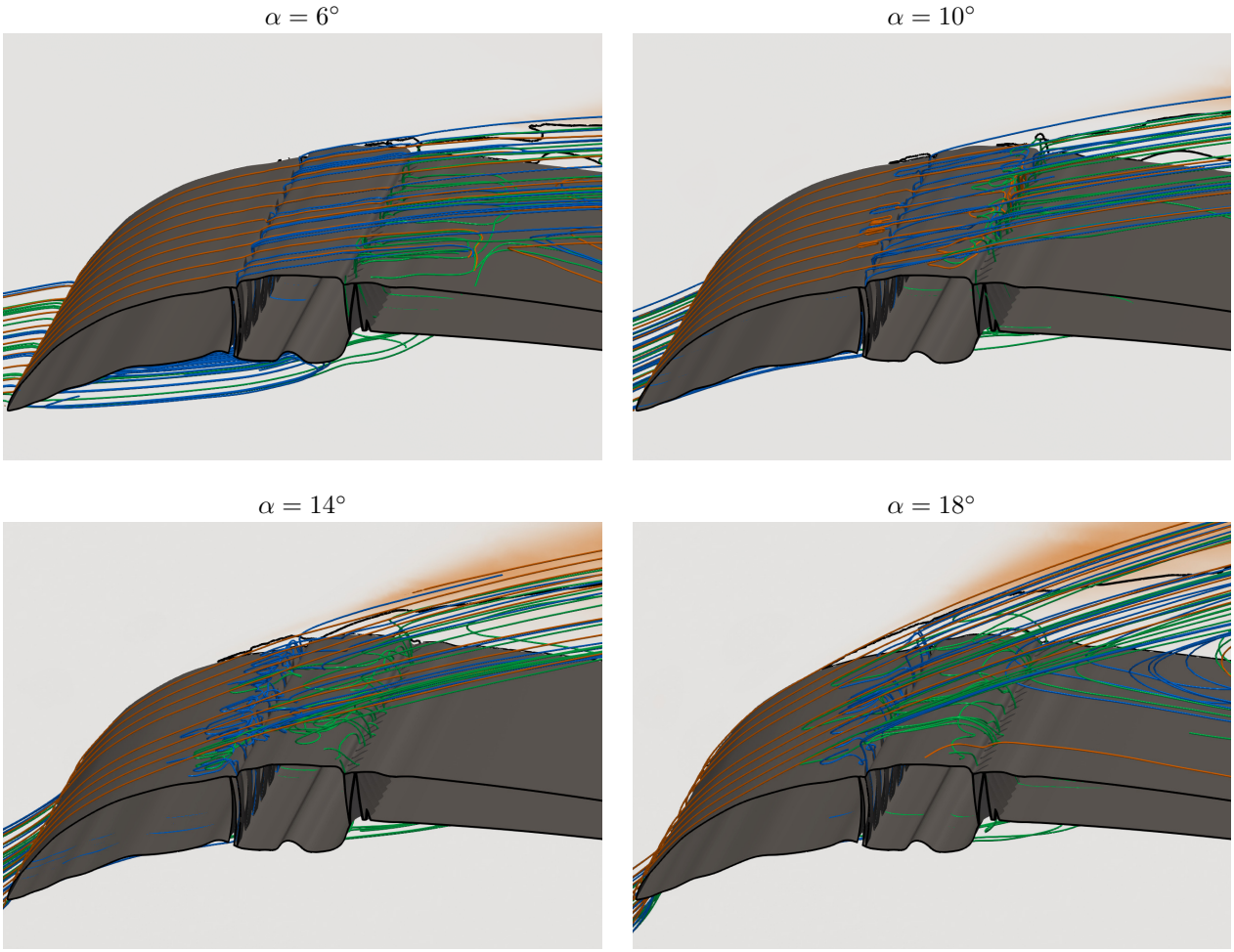

Figure 13: Streamlines around the wing and through the holes. Lines colored orange approach around the leading edge, blue lines pass through the front holes, green lines through the aft holes.

converged in all cases and should not contain significant inhomogeneities in span-wise direction. However, since the streamlines in regions of low velocity magnitude are very sensitive to sidewise components, the streamlines might make the flow field appear less converged than it actually is.

At $\alpha = 6°$, the blue and orange streamlines from leading edge and front holes are perfectly attached until they have passed the shaft. A small recirculation appears immediately downstream of the shaft, which mostly consists of flow from the second row with green streamlines and a very small fraction of flow from the separated shear layer. Above this region, the large major recirculation is formed, in which flow from all streamlines is mixing. On the lower side where the flow separates behind the leading edge, two regions of recirculation form upstream and downstream of the shaft which feed the flow through the corresponding hole rows.

When increasing the angle of attack to $\alpha = 10°$, the main separation moves upstream as discussed above. Some blue streamlines turn slightly upstream but re-attach when reaching the shaft. Then the main separation occurs. All green streamlines from the aft row first point upstream and then mix into the separated shear layer. The small recirculation zone seen at $\alpha = 6°$ does not appear any more. In the higher angles of attack where the flow separates upstream of the shaft, almost all streamlines point upstream after leaving the holes. Most of the lines from the aft row even reach the area upstream of the shaft before mixing into the shear layer. On the lower side, the blue streamlines are attached after passing the leading edge and then directly enter the front row of holes. The green lines first pass the recirculation area downstream of the shaft before entering the holes.

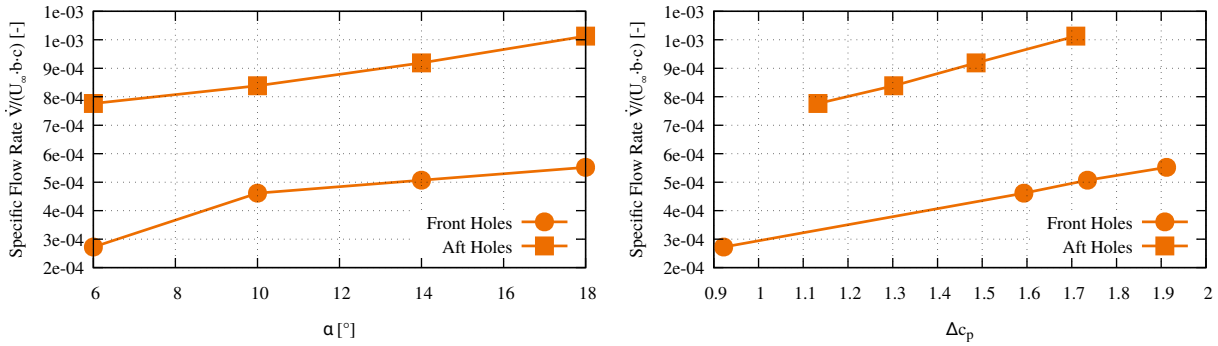

Figure 14: Specific flow rate $\dot{V}$ through the holes per span b, normalized with bulk speed U_∞ and chord length c. Plotted over angle of attack (left) and over pressure coefficient difference (right).

Finally, one key factor to quantify the effect of the holes is the flow rate of air passing the through the holes. Figure 14 shows two plots of the flow rate, namely its dependency on the angle of attack and its dependency on the pressure difference along the holes. The flow rate is presented in a specific formulation with respect to the span width b. Further, it is made dimensionless with freestream speed U_∞ and chord length c to ease scaling to other dimensions.

In the plot over the angle of attack the values appear in a straight line showing a linear dependency besides the flow rate through the front holes at $\alpha = 6°$. This is the only case with separated flow on the lower side of the wing in the front part. Therefore, the flow conditions are different, which primarily affects the pressure difference along the holes. To compensate for this effect, the flow rate also has been plot with respect to the difference of the pressure coefficient, which reveals an almost ideal linear correlation. However, it needs to be noted that the linear regression for the aft holes, unlike the values recorded for the front row, will not reach zero flow rate when the pressure difference vanishes. This supposedly comes from the observation with actual flow around the wing, where strong pressure gradients are present around inlet and outlet and the pressure gradient extracted along the holes might not exactly be the one driving the flow.

The flow rate through the front row is significantly lower than the one through the aft raw. This is obviously caused by the fact that the aft row features twice as many holes as the front row, whereas the cross-sectional area of the individual holes is very similar in both rows. Comparing the same angle of attack, the flow through the aft hole row is 2.85 times higher at $\alpha = 6°$ and 1.82 times higher for the other cases. With respect to the pressure difference, the factor is 2.15 in average.

Eder et al. [6] have performed measurements of flow rate and permeability on a feather. Since their method of measurement cannot be transferred from a real feather to the present CFD model with holes only, a direct and quantitative comparison with their findings is not possible. However, a qualitative assessment shows similar trends. Eder et al. also state a linear dependency on the pressure difference, which can be confirmed from the present simulations. Further, they have found a factor in the range between 1.6 and 2.4 for the ratio of the flow rates from both hole rows. This range also covers the presently found value.

5 Conclusions

Simulations of the flow around a planar airfoil based on a bird feather have been performed to investigate the effect of permeability through hole structures along the shaft. The geometry of the holes has been fully resolved in the computations. The CFD setup allows to study their effect in an isolated way, independently from other features found on a feather like permeable vanes or the surface structure.

It has been shown that while the flow is attached along the lower side of the external vane, the lifting force is increased by the impact of the holes on the flow along the upper side, whereas the efficiency remains almost constant. When the flow separates below the leading edge at lower angles of attack, the gain of lift vanishes but the efficiency is decreased. The effect is mostly attributed to the impact of the jets from the holes on the separated shear layer. It is not strong enough to establish a re-attachment but the shear layer

is slightly bent towards the surface and thereby the level of suction along the upper side increases.

Comparisons of trends for the flow rate with measurements from literature [6] confirm the plausibility of the present findings, even though a quantitative comparison was not possible due to differences in the setup. The results will contribute to the development of a model for the simulation of more realistic feathers at larger scale, where not every single feature of the geometric structure can be resolved.

References

[1] Vance A Tucker. Gliding birds: reduction of induced drag by wing tip slots between the primary feathers. *Journal of Experimental Biology*, 180(1):285–310, 1993.

[2] Marco KleinHeerenbrink, L Christoffer Johansson, and Anders Hedenström. Multi-cored vortices support function of slotted wing tips of birds in gliding and flapping flight. *Journal of the Royal Society Interface*, 14(130):20170099, 2017.

[3] X Pascoe. Nachlaufvermessung eines Storchenflügels. *Institut für Aerodynamik der TU München*, 2009.

[4] Heinrich Eder. Die Bionik der Schwungfederkaskade: Lösung einer Optimierungsaufgabe. *Biologie in unserer Zeit*, 49(1):68–72, 2019.

[5] Eike Tangermann, Gianantonio Ercolani, and Markus Klein. Aerodynamic Performance of Biomimetic Wings in Soaring Flight – a Numerical Study. In *13th Symposium on Engineering Turbulence Modelling and Measurements (ETMM-13), Rhodes, Greece*, 2021.

[6] Heinrich Eder, Wolfgang Fiedler, and Xaver Pascoe. Air-permeable hole-pattern and nose-droop control improve aerodynamic performance of primary feathers. *Journal of Comparative Physiology A*, 197(1):109–117, 2011.

[7] Florian R Menter. Two-equation eddy-viscosity turbulence models for engineering applications. *AIAA journal*, 32(8):1598–1605, 1994.

[8] Robin B Langtry and Florian R Menter. Correlation-based transition modeling for unstructured parallelized computational fluid dynamics codes. *AIAA journal*, 47(12):2894–2906, 2009.

[9] Eike Tangermann and Markus Klein. Numerical Simulation of Laminar Separation on a NACA0018 Airfoil in Freestream Turbulence. In *AIAA Scitech 2020 Forum*. American Institute of Aeronautics and Astronautics, January 2020.